Crystal plasticity modelling and HR-DIC measurement of slip activation and strain localization in single and oligo-crystal Ni alloys under fatigue

Yongjun Guan [a], Bo Chen [b], Jinwen Zou [a], T. Ben Britton [b], Jun Jiang [b, c], Fionn P.E. Dunne [b, c, *]

[a] Materials Genome Center, Beijing Institute of Aeronautical Materials, Beijing, 100095, China
[b] Department of Materials, Imperial College London, SW7 2AZ, UK
[c] Department of Mechanical Engineering, Imperial College London, SW7 2AZ, UK

ARTICLE INFO

ABSTRACT

Single crystal (CMSX4) and oligocrystal (MAR002) nickel have been studied using three-point beam bending under conditions of cyclic loading. SEM images have enabled identification of slip activation, and high resolution digital image correlation has been utilized to quantify the developing strain fields and the strain localization in both single and oligocrystals in fatigue. The single and oligocrystal microstructures have been replicated within crystal plasticity finite element models and the fatigue loading analysed such that grain-by-grain comparisons of slip may be carried out. Single and multiple slip activation, slip localization and microstructure-sensitive stress evolution have been examined.

Single crystal bend fatigue gives rise to non-symmetric slip fields and localization depending on crystallographic orientation. Modelling correctly captures slip activation and the developing non-symmetric slip fields. Oligocrystal slip is markedly heterogeneous, with grain misorientations driving strong variations, also reasonably captured by the model. Microstructure behaviour is found to vary spatially and include elastic-plastic hysteresis which is stable, and which undergoes mean stress relaxation so that plastic shakedown occurs. Remarkable variations occur between locations either side of grain boundaries, providing appropriate opportunities for fatigue crack nucleation.

1. Introduction

It is increasingly recognized that the nucleation of defects and cracks during fatigue consumes a considerable fraction of engineering component life relative to the propagation of cracks. In addition, the latter is deemed to be reasonably well understood, particularly in the sense of obtaining useful quantitative prediction of safe component lifetimes. The same cannot yet be said of fatigue crack nucleation for which mechanistic understanding has remained elusive and as a consequence, a paucity of predictive capability exists leading often to highly conservative and hence expensive safe-life component design.

* Corresponding author. Department of Materials, Imperial College London, SW7 2AZ, UK.
  E-mail address: fionn.dunne@imperial.ac.uk (F.P.E. Dunne).

Fatigue crack nucleation is complex and appears to be inextricably linked to microstructure. A wide variation in microstructural features in differing material systems exists; for example, in the nickel alloys containing annealing twins, fatigue crack nucleation has been associated with twin boundaries (Stinville et al., 2015; Sangid et al., 2011a, 2011b; Miao et al., 2009). In the powder metallurgy nickel alloys (increasingly employed in the aero-industry) however, oxide agglomerates are known to develop and to provide a key role in defect nucleation under fatigue through agglomerate-nickel matrix decohesion (Zhang et al., 2016; Huron and Roth, 1996), agglomerate fracture (Zhang et al., 2015a), or through slip localization and crack nucleation (Jiang et al., 2016a; Hyzak and Bernstein, 1982; Bonacuse et al., 2002; Shenoy et al., 2005a). In this alloy system alone, four major origins of fatigue crack nucleation may be identified. Correspondingly, the range of mechanisms in steels is similarly wide. In 316 stainless, for example, nano-scale dislocation ladder structures have been observed with slip localization and the establishment of persistent slip bands (PSBs) as precursors to fatigue crack nucleation (Pham and Holdsworth, 2013). In the martensitic steels, the complex lath structures provides significant mis-match in elastic properties and hence considerable constraint effects leading to multiaxial stress states at the microstructural level coupled with complex interfacial decohesion and lath brittle fracture processes (Li et al., 2016). Fatigue crack nucleation in ferritic steels has been observed to be associated with the establishment of slip localization at free surfaces. This is influenced strongly by the elastic anisotropic mismatch associated with the bcc crystallography giving rise to stress states favorable for slip activation and subsequent localization (Sweeney et al., 2013). In a range of the aero-industry titanium alloys, fatigue crack nucleation is dwell sensitive and observed to be associated with hcp crystal basal planes, often in combination with a crystallographic orientation pairing with an adjacent grain giving rise to worst-case stress redistribution sufficient (with other factors) to drive basal facet nucleation (Dunne et al., 2007a; Dunne and Rugg, 2008; Rugg et al., 2007). Interestingly, the rate-sensitive response of the material is a key factor in the crack nucleation process (Zhang et al., 2015b; Dunne et al., 2007b).

The above discussion serves only to explain why the phenomenon of fatigue crack nucleation remains complex and the mechanistic basis broad across the metal alloys of structural significance. However the complexity should not, it is argued, inhibit the search for a unified understanding of fatigue crack nucleation and consequently, much research is carried out with this objective across material systems, length scales and techniques. In the present work, we focus on arguably simple nickel alloys since they provide the basis for efficient flight and power generation utilized in gas turbine engines. The micron length scale chosen is that of the key microstructural features, namely grains, crystallography, morphology and boundaries, and the techniques bring together small-scale testing, high-resolution digital image correlation (DIC) and crystal plasticity modelling. A related approach was presented by Lim et al. (2014) who carried out detailed studies of strains, rotations and texture evolution in a coarse-grained tantalum oligocrystal providing grain by grain comparisons of DIC measurements and crystal plasticity calculations. The oligocrystal samples studied were subjected to monotonically increasing strain and it was found that the crystal plasticity model provided reasonable quantitative predictions of the HR-DIC measured strains and rotations. Our focus in this work, however, is in *cyclic* loading in simple Ni systems in which significant strain accumulation occurs, leading to localization as a result of the cycling. Further, in addition to utilizing HR-DIC and accurate realisations of single and oligocrystal geometries in crystal plasticity models, we also employ SEM to provide detail on slip system activation and the spatial distributions of the activation within the single and oligo-crystals.

Significant work has been carried out in nickel alloys fabricated through powder metallurgy methods which may contain oxide agglomerates ranging from 10 to 200 μm in size. When subjected to cyclic plasticity, the agglomerates act as preferential sites for crack nucleation and when present, become the key microstructural feature relevant to defect nucleation as opposed to twin boundaries (Hyzak and Bernstein, 1982; Gabb et al., 2002; Shenoy et al., 2005b; Denda et al., 1992). The importance of the recognition of the key features of microstructures which drive crack nucleation is argued to be a crucial factor in establishing successful quantitatively predictive techniques. Recent work (Zhang et al., 2016; Zhang et al., 2015a; Jiang et al., 2015, 2016a) has shown using high-resolution electron backscatter diffraction (EBSD) and DIC that the agglomerates act to localize slip leading to PSB formation and that under cyclic loading, local ratcheting occurs leading to very significant inhomogeneity across the microstructure but also, to strain levels in excess of 10% local to the agglomerate, far in excess of the macroscale strain levels imposed. Studies also show that high densities of geometrically necessary dislocations (GNDs) develop particularly at the agglomerate but across the microstructure driven by other discontinuities such as grain boundaries (Jiang et al., 2015). Defect nucleation occurs by oxide agglomerate fracture (Zhang et al., 2015a), by oxide/nickel matrix decohesion (Zhang et al., 2016), and by PSB formation local to the agglomerate (Jiang et al., 2016a). Residual stresses resulting from the thermal mismatch between agglomerate and nickel matrix have also been assessed (Zhang et al., 2014) and their implication in subsequent in-service cyclic plastic behaviour was analysed (Zhang et al., 2016). It has been concluded that key mechanistic drivers for defect nucleation in these nickel alloys include the establishment of slip, high GND densities, and high stress. However, it is very apparent from the experimental studies (Zhang et al., 2015a; Jiang et al., 2015, 2016a) that no one mechanistic driver in its own right (say local slip, or GND density) definitively and exclusively determines the location of fatigue crack nucleation (with the exception of interfacial normal stress in the context of oxide/nickel matrix decohesion (Zhang et al., 2016)). A quantity for which the evidence increasingly demonstrates does, however, is the local stored energy density — the elastically stored energy per unit area resulting from dislocation structure (i.e. where dislocation interaction stresses are not negligible) (Wan et al., 2014, 2016; Jiang et al., 2016a).

Certainly for the nickel alloys discussed above, and likely more broadly across other metal alloys, key factors in fatigue crack nucleation are the localization of slip, the formation of PSBs, the progressively increasing slip accumulation and plastic strain gradients, the consequent GND density and hence stress, culminating in high local stored energy, a Griffith-like quantity. The microstructural features driving these mechanisms and dominating fatigue response may be twins, grain

boundaries, agglomerates, second-phase particles, or dendrites for example. But clearly in order to understand the mechanistic basis of crack nucleation, the mechanistic factors need to be identified, assessed and modelled in order to provide quantitative predictive capability. This paper addresses this in the context of some 'simple' single crystal and oligocrystal nickel alloys which are subjected to bending fatigue testing combined with high resolution DIC and microstructurally replicated within crystal plasticity modelling. Slip activation and accumulation and localization in boundary-free (single crystal) and constraint-affected (oligocrystal) samples are examined under cyclic loading. Observed and predicted slip system activity, slip localization and accumulation is assessed and quantified in order to provide validated predictive modelling both within the bulk of individual grains but importantly also at boundaries. The experimental and crystal plasticity modelling methodologies are described in the next section, followed by the presentation of cyclic beam results in single crystal CMSX4 and in (directionally solidified) oligocrystal alloy MAR002.

2. Methods

2.1. Materials and experimental three-point bend testing

Three-point macroscopically R = 0 load-controlled tests are carried out on beam samples (of dimension $12 \times 3 \times 3$ mm) in order to provide a confined region of high macro-scale stress local to a free surface where fatigue crack nucleation is preferable. The same sample geometry was utilized for both the single crystal nickel CMSX4 alloy, for which two differing non-[100] crystallographic orientations with crystal orientations of [244° 32° 141°] and [85° 5° 263°] respectively were examined, and the MAR002 oligocrystal material, for which two differing microstructures were studied. The latter oligocrystal alloy was directionally solidified and provided by Rolls-Royce to produce a pseudo-two dimensional morphology with prismatic grains (in both the morphological and crystallographical senses), with the loading applied normal to the prismatic grain geometry. Crystallographic orientation and grain morphology (where appropriate) were obtained using EBSD on the (front) free surface of the samples, and high-resolution DIC was carried out on the (back) free surface, with both of these surfaces parallel to the loading direction. A schematic diagram of the experimental set-up for the case of a single crystal test is shown in Fig. 1.

The loading is also shown in Fig. 1 indicating its cyclic nature and that also, the maximum load, F, applied in each cycle is progressively increased in order to ensure continued accumulation of slip from cycle to cycle. The sample bottom free surface remains clear and unaffected by application of loading on the top surface so that slip activation and localization is microstructurally driven within the region of higher bending stress developed by the three-point loading configuration.

Both single and oligocrystal alloys are FCC in crystal structure and to facilitate analysis, a consistent slip system nomenclature has been defined and shown in Fig. 2.

Both the CMSX4 and MAR002 single and oligo-crystal materials respectively contain a fine distribution of γ' particles with associated micron length scale. An independent micro-pillar compression test was carried out on a sample ($\sim 5 \times 5 \times 20$ μm) of the CMSX4 single crystal at room temperature which established that once γ-phase slip had initiated, it was not visibly affected, either in direction or rate, by the γ' phase as the latter was cut by the active slip system. Similar observations were made by Huskins et al. (2015). The oligocrystal grain size is large and ~ 3000 μm such that the strain heterogeneity developed by the three-point loading and the grain boundary constraint-affected regions are large compared to the γ' particle size.
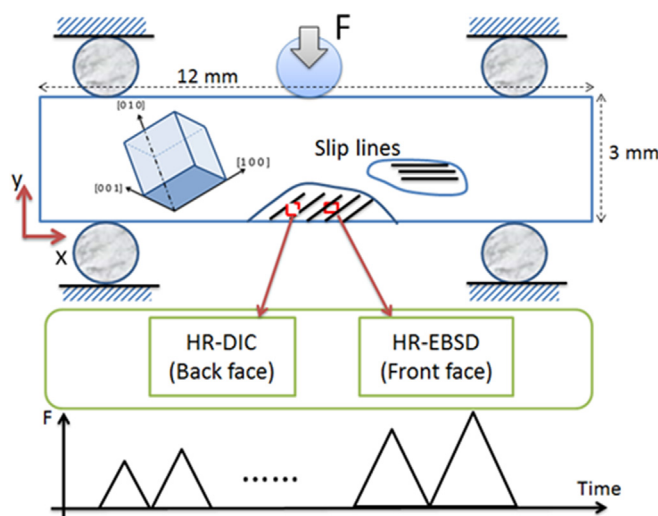

Fig. 1. Schematic diagram showing the single-crystal three-point beam loading identifying the key regions of interest for slip, the anticipated predominant slip activity, the locations and beam faces at which HR-DIC and HR-EBSD characterization have been carried out, and finally, the progressively increasing load cycles applied.
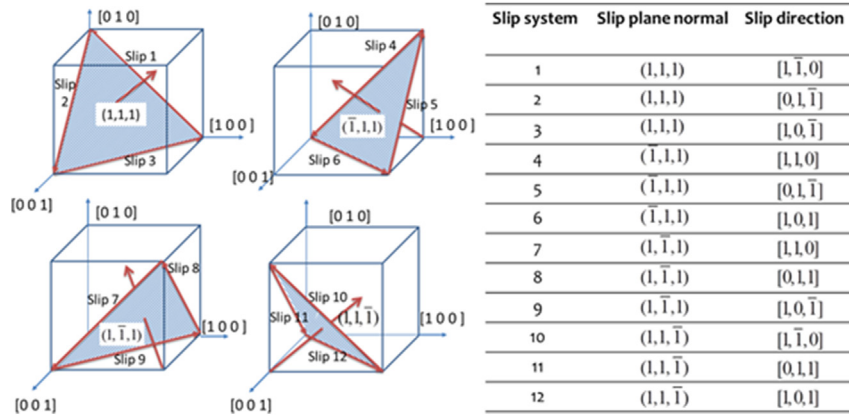
Slip system	Slip plane normal	Slip direction
1	$(1,1,1)$	$[1,\bar{1},0]$
2	$(1,1,1)$	$[0,1,\bar{1}]$
3	$(1,1,1)$	$[1,0,\bar{1}]$
4	$(\bar{1},1,1)$	$[1,1,0]$
5	$(\bar{1},1,1)$	$[0,1,\bar{1}]$
6	$(\bar{1},1,1)$	$[1,0,1]$
7	$(1,\bar{1},1)$	$[1,1,0]$
8	$(1,\bar{1},1)$	$[0,1,1]$
9	$(1,\bar{1},1)$	$[1,0,\bar{1}]$
10	$(1,1,\bar{1})$	$[1,\bar{1},0]$
11	$(1,1,\bar{1})$	$[0,1,1]$
12	$(1,1,\bar{1})$	$[1,0,1]$

Fig. 2. Identification of FCC slip directions and normals, and slip direction number designations utilized throughout the paper, shown with respect to an orthogonal (x, y, z) reference system.

Hence the γ′ particles are not explicitly considered in this work; particularly, they are not explicitly represented in the crystal plasticity model reconstructions of the tested microstructures, and analysis of local slip subsequently shows this to be a reasonable simplification. There was some evidence of dendrite formation, particularly associated with the oligocrystal samples, but these regions were not found to affect the observed slip fields developing any differently within a given grain. Subsequent analysis by high-resolution EBSD showed that the dendrite regions did cause small perturbations in the fields of GND densities to be developed, but in the samples considered in this paper, these regions were well removed from the regions of interest and relevant to free-surface fatigue crack nucleation.

2.2. High resolution DIC for strain measurement

DIC strain measurement requires a random speckle pattern of fine colloidal silica particles (of size ~50−250 nm) to be applied to the region of interest on the back free surface of the samples, as indicated in Fig. 1. After pre-selected cyclic intervals, the sample was removed from the loading rig and secondary electron imaged (again) in a Zeiss Auriga SEM using high beam current at 20 KeV for the DIC measurement. It should be noted that in practice, reinserting samples back into the rig with precise alignment is difficult. Care was taken to reinsert the samples by ensuring that the deforming region of interest aligned with the loading head through the DIC camera.

To perform the correlation, the images were divided into sub-sets of selected areas, which were individually related to the reference (the initially undeformed state) to give in-plane displacements using an in-house image based cross-correlation method. Band pass filters capable of removing high and low frequency noise raised from background variation were applied. Components of in-plane total strains were obtained by differentiating the displacement field. The size of the colloidal silica particles (50−250 nm) providing fine DIC patterning, allowed SEM imaging at high magnification. Compared with the average grain sizes in the oligocrystals, the applied sub-set sizes are much smaller, enabling sub-grain strain resolution to be achieved. After the initial sample characterization, application of the speckle pattern and acquisition of the reference image, the samples were fatigued under force-controlled loading at a frequency of 0.023 Hz with a triangular waveform. The tests were performed with a maximum force of 3000 N (depending on the sample type) and a rate of 100 Ns^{-1} on a Zwick Roell Z010 load frame (see Fig. 3 for an example). The testing was interrupted at selected cyclic intervals, and the sample removed from the rig in order to capture deformed images for DIC strain measurement.

The complete underlying crystal orientation distribution of the beam was characterized by a Bruker EBSD system at step size of 2 μm. The EBSD camera exposure time (0.01s) and binning size (8 × 8) were optimized for scanning rate. No noise reduction function was applied to artificially manipulate the unindexed points.

The three-point beam cyclic test methodology, DIC strain measurement and EBSD for orientation mapping in the context of a range on nickel alloys have been reported in detail elsewhere (Zhang et al., 2016; Zhang et al., 2015a; Jiang et al., 2015, 2016a) so are summarized here briefly in this paper for completeness only.

2.3. Crystal plasticity finite element modelling

In the crystal plasticity framework, the deformation gradient, **F**, is multiplicatively decomposed into elastic, **F**$_e$, and plastic, **F**$_p$, parts where the elastic contribution captures the lattice stretch and rigid body rotation and the latter plastic term governs slip

$$\mathbf{F} = \mathbf{F}_e \mathbf{F}_p. \tag{1}$$

F is determined explicitly from displacements and contains information on stretch, slip and rigid body rotation. The total rate of deformation, **D**, is written as the sum of elastic and plastic rates of deformation as follows

$$\mathbf{D} = \mathbf{D}_e + \mathbf{D}_p \tag{2}$$

in which $\mathbf{D}_e$ is determined from anisotropic Hooke's law, and $\mathbf{D}_p$ from the plastic velocity gradient, $\mathbf{L}_p$, using

$$\mathbf{D}_p = \text{sym}(\mathbf{L}_p) \tag{3}$$

which in turn is given as the sum of contributions to slip from the active systems such that

$$\mathbf{L}_P = \sum_{i=1}^{n} \dot{\gamma}^i (\mathbf{s} \otimes \mathbf{n}) \tag{4}$$

where $\dot{\gamma}^i$ is the rate of dislocation slip on the ith slip system with slip direction, **s**, and slip plane normal, **n**. The physically-based slip rule giving the slip rate on slip system used within this study accounts for dislocation motion overcoming pinning obstacles by means of thermal activation and has been well reported and utilized for nickel alloys (Zhang et al., 2016; Zhang et al., 2014; Wan et al., 2016; Dunne et al., 2007c):

$$\dot{\gamma}^\iota = \rho_{SSD}^m b^2 \nu \exp\left(-\frac{\Delta H}{kt}\right) \sinh\left(\frac{(\tau^\iota - \tau_c)\Delta V}{kT}\right) \tag{5}$$

where ρ_{SSD}^m is the density of gliding dislocations, b the magnitude of Burgers vector, ν the frequency of jumps to overcome obstacle barriers, successful or otherwise, ΔH Helmholtz free energy, k the Boltzmann constant, T the temperature in Kelvin, and ΔV the activation volume.

Isotropic hardening based on Taylor's dislocation hardening is assumed in the slip rule and shown in (6) where G is the shear modulus, ρ_{SSD}^s the density of sessile statistically stored dislocations, and τ_0 the initial critical resolved shear stress. The hardening rate on each of the 12 FCC slip systems is taken to be the same.

$$\tau_c = \tau_0 + Gb\sqrt{\rho_{SSD}^s}. \tag{6}$$

The density of the statistically stored dislocations is determined using a phenomenological relation with effective plastic strain, p, based on experimental observation of the crystal hardening and is given by Equation (7)
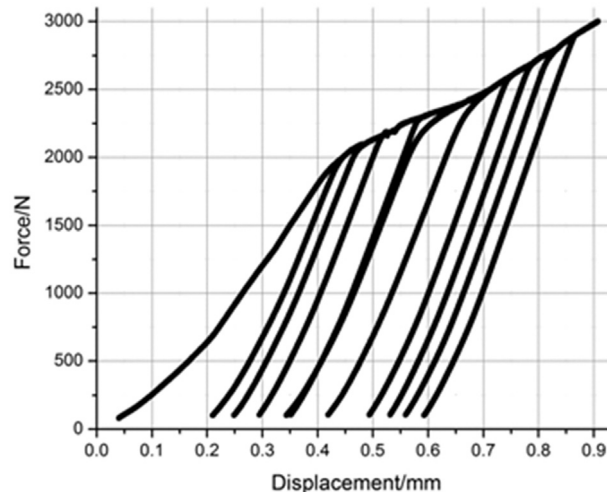

Fig. 3. The experimentally measured load-displacement curves obtained for single crystal nickel alloy beam sample 1 under progressively increasing (cycle to cycle) force-controlled loading.

Table 1
Material parameters and physical properties for the nickel-based superalloy slip rule.

ρ_{SSD}^{m}	$0.05\ \mu m^{-2}$
b	$3.51 \times 10^{-4}\ \mu m$
ν	$1.0 \times 10^{11}\ s^{-1}$
ΔH	$4.913 \times 10^{-20}\ J$
ΔV	$0.237 b^3$
k	$1.38 \times 10^{-23}\ J\ K^{-1}$
τ_c	350 MPa
λ	$200\ \mu m^{-2}$

$$\dot{\rho}_{SSD}^{s} = \lambda \dot{p} \tag{7}$$

in which λ controls the rate at which the dislocation density evolves and the rate of effective plastic strain is related to the rate of plastic deformation by

$$\dot{p} = \left(\frac{2}{3} \mathbf{D}_p : \mathbf{D}_p \right)^{1/2} \tag{8}$$

The properties arising in the slip rule have been obtained from the literature (the anisotropic elastic stiffnesses, Burger vector magnitude, Boltzman constant, representative initial mobile dislocation density) or from comparison of the crystal
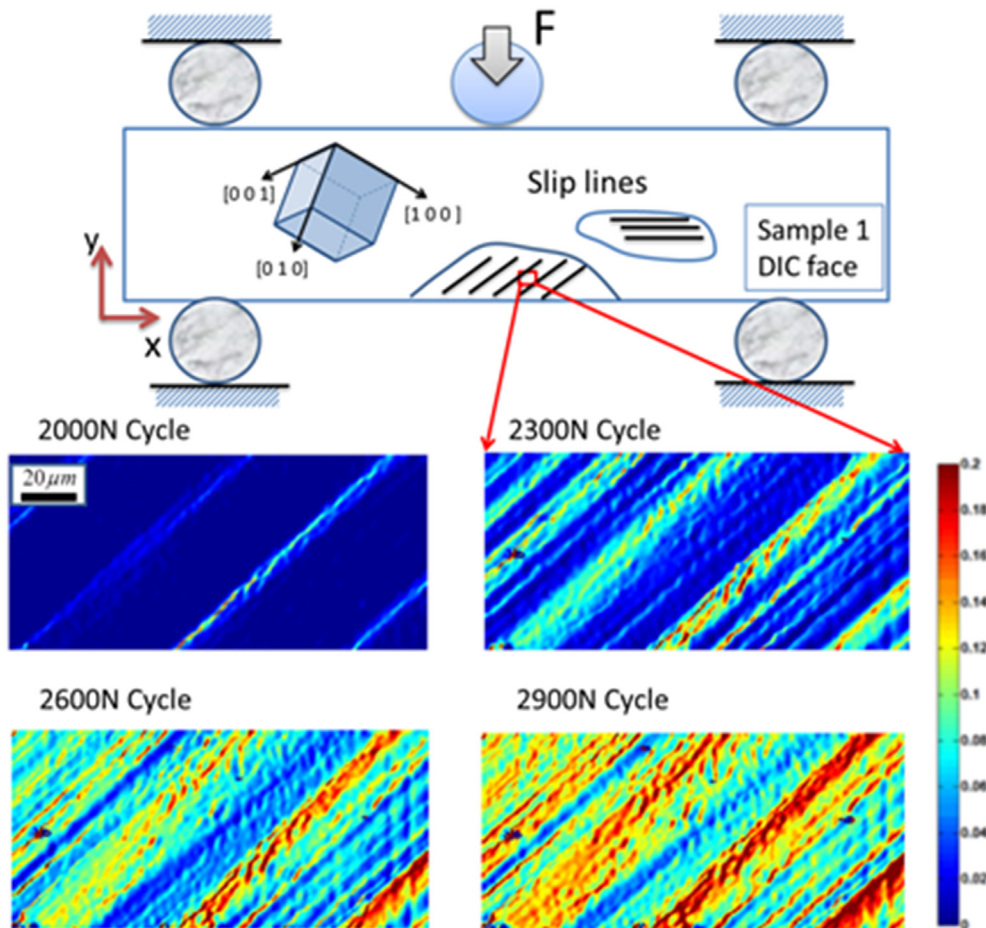

Fig. 4. HR-DIC measured ε_{xx} strains for single crystal beam sample 1 with crystallographic orientation shown at the particular region of interest indicated, for the loading cycles with peak applied forces of 2000, 2300, 2600 and 2900 N respectively, given in Fig. 3.
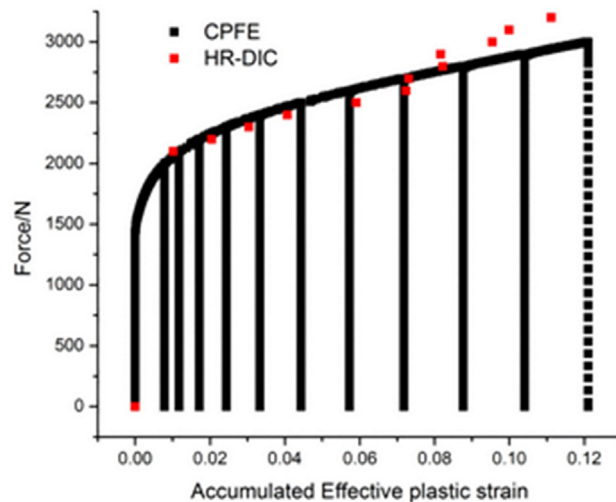
Fig. 5. Experimentally (HR-DIC) measured and crystal plasticity finite element (CPFE) determined accumulated plastic strain corresponding to the cycles shown, obtained by averaging the measured and predicted strains over the region of interest shown in Fig. 4.

plasticity model with the first single crystal beam test carried out (and detailed later). The full set of properties in the slip rule are listed in Table 1. The Helmholtz free energy ΔH was chosen to generate undetectable rate sensitivity at the applied rate of loading ($\sim 4.82 \times 10^{-3}s^{-1}$) whilst being physically reasonable.

3. Single crystal fatigue: experimental observations and crystal model predictions

The test sample designated single crystal sample 1 is shown schematically in Fig. 1 with the crystallographic orientation indicated and has been subjected to cyclic mechanical loading with progressively increasing load shown in Fig. 3. In this figure, the force indicates the applied load provided by the roller shown in Fig. 1, and the displacement is that of the top surface of the sample in contact with the loading roller.

The first loading cycle shows considerable nonlinearity resulting from the bedding in of the sample within the loading rig. Subsequent loading cycles, reflecting the imposed R = 0 cyclic bending, are consistent and show an elastic response followed by nonlinear plastic behaviour. On unloading, at low applied force, there is some evidence of nonlinear behaviour which, because of the absence of hysteresis, is ascribed to the loading rig. The progressively increasing applied loading is clearly visible and the resulting macroscale progressive accumulation of displacement is also very evident. The DIC measurements enable the quantification of the strains on the back surface of the sample shown in Fig. 1, and example DIC strain measurements are shown in Fig. 4 at the loading cycles indicated. Note that because of the back surface view of the sample, the crystallographic orientation shown in Fig. 4 is reversed compared to that in Fig. 1.

The DIC measured xx-strains show strong localization early in the cyclic history with discrete, well-separated bands of slip developing, indicative of predominantly single slip taking place in the crystal. A detailed analysis of the nature of the slip and its compatibility with the strain and beam deformation has recently been provided in (Jiang et al., 2016b). As cycling proceeds, while the spacing between predominant bands of slip remains the same, much secondary parallel slip is activated, with the effect of smearing, or distributing more evenly, the developing strains. This is occurring because of the hardening of initially activated slip systems tending to prefer the activation of softer adjacent slip planes to redistribute the overall strain. At the cycle corresponding to applied load of 2900 N, that is, the 10th cycle shown in Fig. 3, some locations in the region of interest in Fig. 4 show strains of ~2%, but adjacent locations with much higher slip give rise to strains of ~20%, indicating remarkable heterogeneity in the slip field. The strains given in the region of interest in Fig. 4 may be averaged and shown against the measured applied load in order to give the scale of plastic strain accumulation taking place. The strain components obtained at all DIC grid points overlapping the sample ROI speckle pattern have been extracted and number-averaged at each cycle for which DIC measurements were made. From the averaged strain components, the effective strain was then determined and this quantity is shown in Fig. 5 for each of the DIC measurement cycles. In this particular test, with progressively increasing cyclic loading, significant strain accumulation is anticipated. The abnormal behaviour in the 4th re-loading curve shown in Fig. 3 is due to the re-alignment difficulty when the sample is re-inserted into the testing rig, leading to yielding commencing at a slightly lower applied load, giving rise to the differing behaviour seen on the 4th re-loading at the higher load.

A crystal plasticity finite element model of the single crystal beam shown in Figs. 1 and 4 with the same boundary and loading conditions has been developed. The crystallographic orientation of the single crystal measured from EBSD has been reproduced in the model with the slip rule given in Equation (5). Because the crystal axes are not collinear with the principal axes of beam loading shown in Fig. 4, considerable heterogeneity is anticipated over and above that from the three-point bend
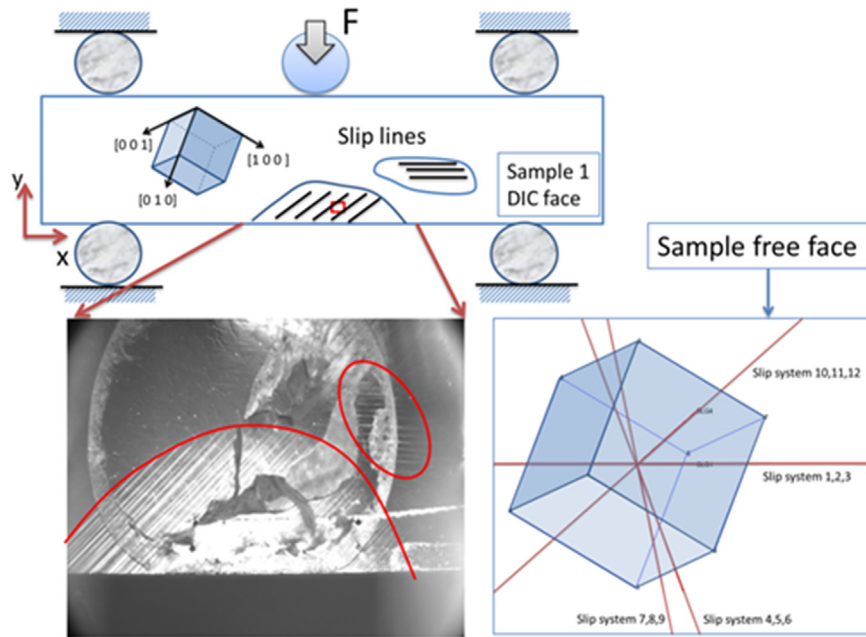
Fig. 6. Experimentally observed SEM free-surface slip line distributions obtained for single crystal sample 1 with crystallographic orientation shown on the DIC sample face. Inset are shown the crystal slip plane intersections with the sample free surface identifying the observed slip system activity.

loading imposed. Hence, in the finite element model of the single crystal beam (and in subsequent oligocrystal analyses), a very refined finite element mesh comprising > 200,000 20-noded, reduced integration (8 integration point) three-dimensional quad elements is developed with five elements through the beam specimen thickness. The experimentally measured data shown in Fig. 5 is utilized in order to refine the slip rule properties, given in Table 1, to give the best representation of the experimental measurements in Fig. 5 by the model. The resulting crystal plasticity model determined load-plastic strain history is thus shown by the black line in Fig. 5. For consistency, the computed plastic strains are obtained from the location in the beam model corresponding to the region of interest where averaged experimentally measured strains are obtained. Note that the crystal model unloading curves are vertical because plastic strains are shown and the DIC images were captured at the unloaded state. Up to about cycle 9, the crystal model accumulated strains are in good agreement with the experimental measurement. Subsequently, agreement is less good, but at this stage in the loading, the deformations are very considerable, and cross-slip and latent hardening are likely to occur in the crystal sample which are not captured in the model. Hence we focus on cycles prior to this loading for the examination of slip activity.

Fig. 6 shows an SEM image of the (back) free surface of the single crystal sample in which the development of slip lines is very clear, and for the large bottom central region within which the DIC was carried out, very much consistent with the DIC-measured slip in Fig. 4. Note in Fig. 6 the very clear demarcation between slipped and non-slipped regions reflecting the three-point beam loading. Note also the slight asymmetry developing in the slip field resulting from the misorientation of the crystal principal axes with the sample loading axis. Fig. 6 also interestingly shows a secondary region of slip in the SEM image offset from the primary region already discussed and highlighted with a red ellipse, indicating the activation of a very different slip family in what is intuitively an unexpected location near to the beam neutral axis. Adjacent to the SEM image in Fig. 6 is shown the projection of the labelled slip systems into the free surface which indicates that the primary slip near the bottom of the beam is one (or more) of the family of 10, 11, 12 systems while the secondary region near the neutral axis must be one of the slip system family 1, 2 or 3 (Slip system nomenclature is given in Fig. 2.). The crystal plasticity model analysis demonstrates that the primary slip is that from slip system 10 (with a small contribution from 11) and that for the near-neutral axis slip from system 3 alone, and the details of the slip fields are shown in Fig. 7. Slip system 10 is well-orientated for slip with respect to the bending (xx) stress and is activated leading to the near-symmetric field in the anticipated region of the single crystal beam. Slip system 3, however, is not well orientated with respect to the direct bending (xx) stress but because the crystal beam has relatively low aspect ratio for bending (12/3 = 4), the shear stress which is maximum at the neutral axis is sufficiently large to activate system 3 which is well orientated for horizontal shear. However, it is very non-symmetric with respect to the beam vertical centre line and the shear stress to the left of the beam centre is not sufficient to activate slip system 3. The non-symmetric development of slip system 3 with progressive loading is shown in Fig. 7, showing good agreement with the SEM slip observations.

A similar SEM slip analysis compared to crystal plasticity prediction may be carried out for the front free surface of the sample, as shown in Fig. 8. Systems 10 and (to a limited extent) 11 are again active as observed from SEM and predicted by the
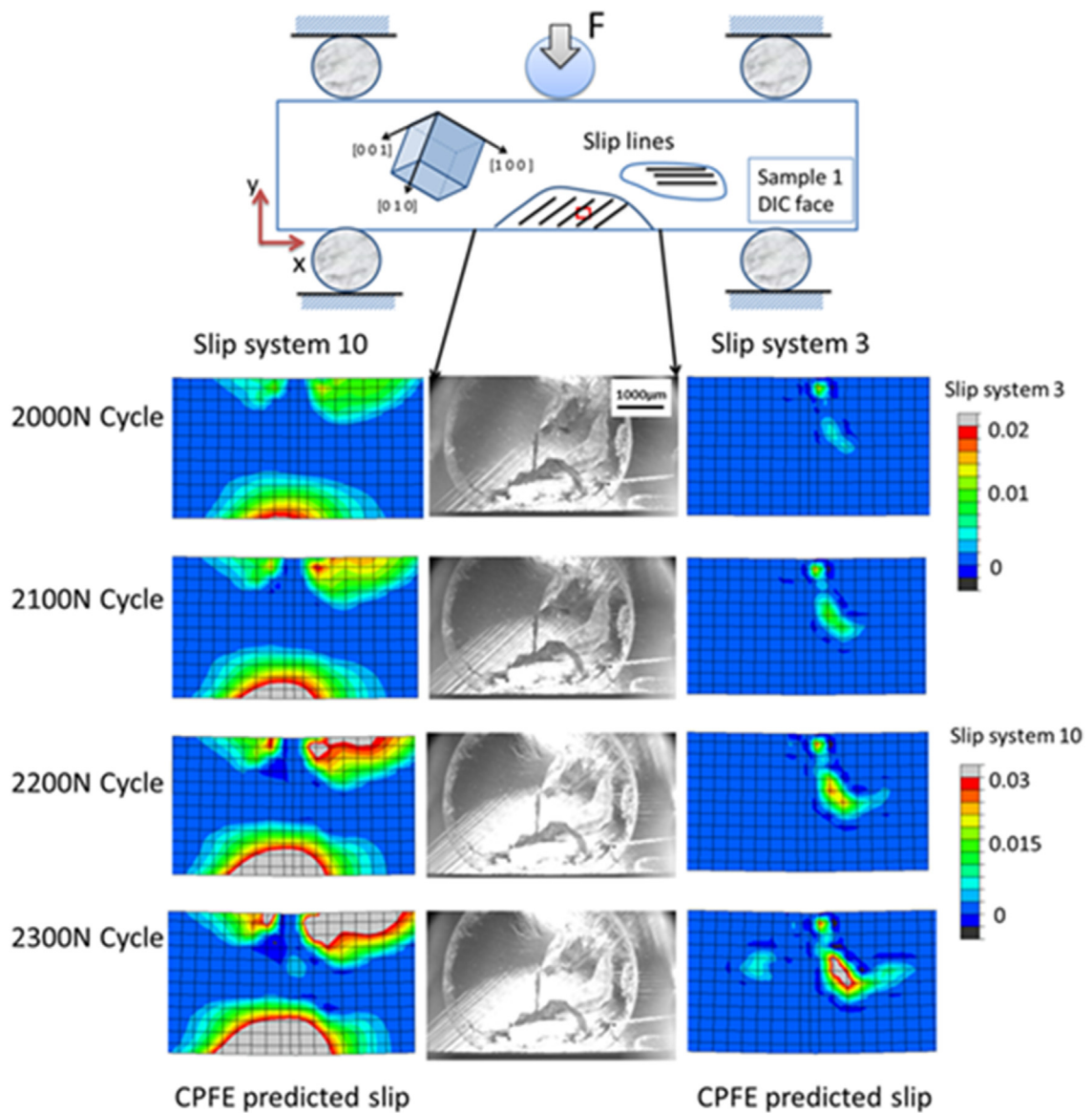
Fig. 7. Comparison of experimentally measured and crystal plasticity predicted slip fields for single crystal sample 1 on the DIC face. Slip systems 3 and 10 shown in Fig. 6 are found to predominate, and their spatial distributions are well-captured by the crystal plasticity model. The asymmetric distribution of slip system 3 results from the crystal orientation with respect to loading.

model. Slip system 3 is predicted as before but because the view is now that from the front free surface (EBSD face), the location of system 3 activity appears reversed in Fig. 8 with respect to that in Figs. 6 and 7. Note that as the crystal deforms, both beam and crystal lattice rotation occur which result in a crystal orientation gradient across the entire sample. Hence obtaining complete coincidence of experimental observed slip line directions with those from the simulation is pragmatically rather difficult and thus a slight offset is seen in Fig. 8.

A further single crystal sample 2 is also briefly assessed before moving on to oligocrystal beams. This sample of CMSX4 has different crystallographic orientation with respect to the loading direction such that very different slip system activation and localization of strain is anticipated. The beam crystallography, activated slip from SEM images and crystal plasticity predictions are shown in Fig. 9.

The optical image of the single crystal beam shows the extent of the slip activity observed, demarcated by the blue line. The slip distribution is immediately seen to be very non-symmetric. Inset SEM figures show the detail of the observed slip activity and slip system 12 is found to predominate in the main region of slip. However, some evidence of slip from systems 1, 2 and 7 is observed and predicted by the crystal model. The asymmetry in the slip field in the optical image is captured particularly well by the crystal model.
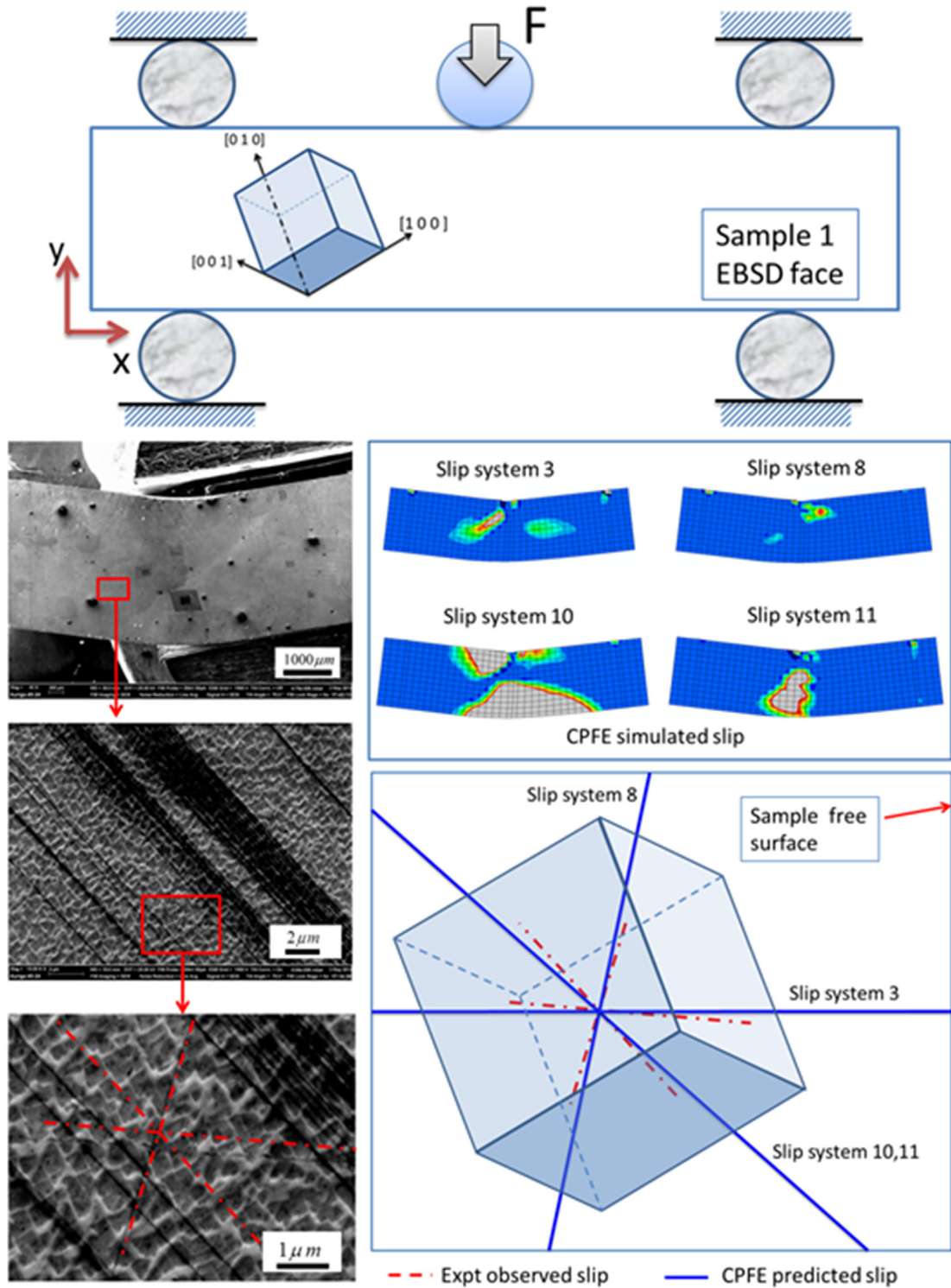
Fig. 8. Comparison of experimentally (HR-DIC) measured and crystal plasticity predicted slip fields for single crystal sample 1 on the EBSD face. Slip systems 10, 11 and 3 and their intersection with the sample free surface are shown in the inset and are found to predominate, and their activation and spatial distributions are well-captured by the crystal plasticity model.
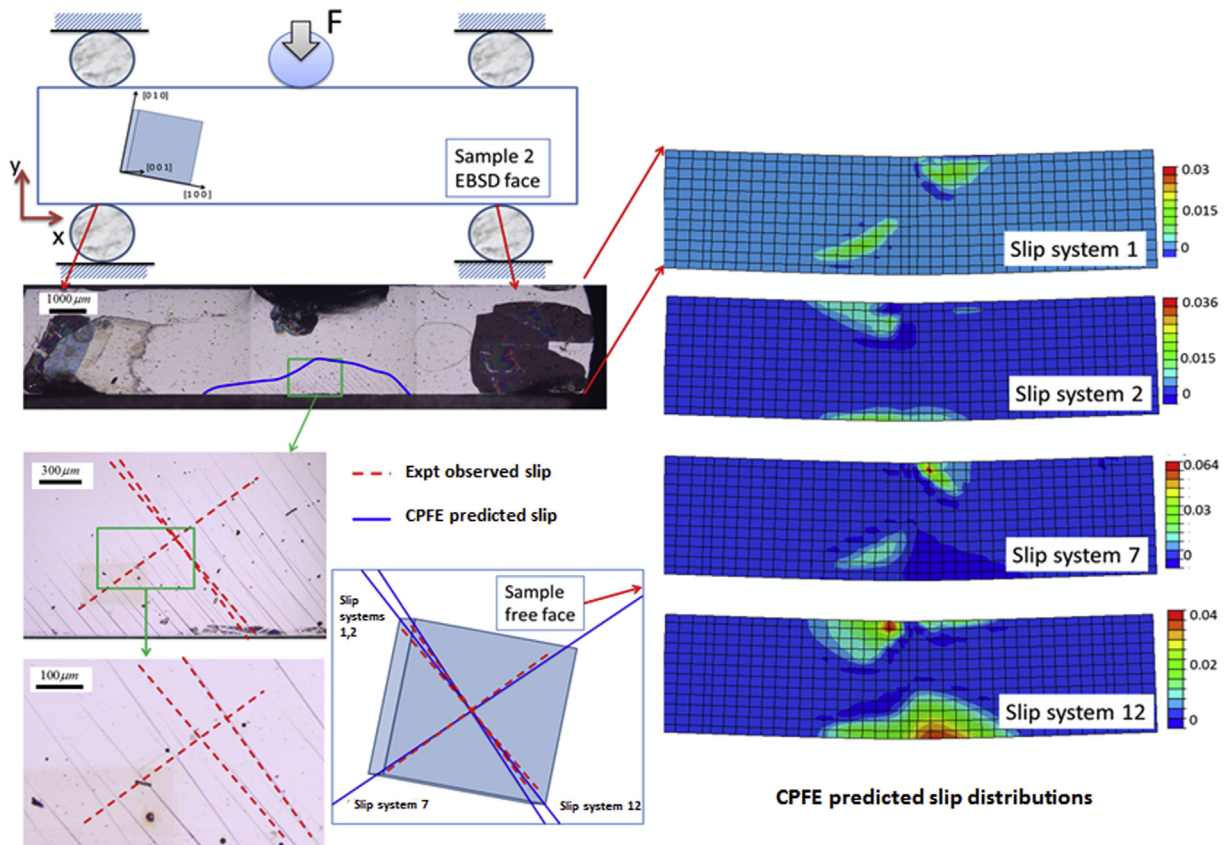
Fig. 9. Comparison of experimentally observed and crystal plasticity predicted slip distributions for single crystal sample 2 on the EBSD face. Slip systems 1, 2 and 12 and their intersection with the sample free surface are shown in the inset and are found to predominate, and their activation and spatial distributions are well-captured by the crystal plasticity model.

The results of the two single crystal beam tests demonstrate the heterogeneity of slip system activation depending on crystallographic orientation, and the asymmetry in strain accumulation which results also from crystal orientation with respect to the loading direction. They also indicate that crystal plasticity modelling captures the slip system activation heterogeneity, the distributions of single and multiple slip, the demarcations between slipped and unslipped regions of the crystal, and the asymmetry of the slip which results from crystal orientation with respect to the principal loading direction. But what happens when grain boundaries are introduced, developing constraints and local stress states very different to those at the macroscale? This is addressed in the next section.

4. Oligo-crystal fatigue: experimental observations and crystal model predictions

The oligocrystal beam samples have the same geometry as that for the single crystal beams and an example is shown in Fig. 10.

The oligocrystal samples are large grained with grain boundaries and crystallographic orientations (details below) indicated by the grain ID map. The region of interest (ROI) is at the top of the front free surface which is free from the effects of direct contact loading from the bottom, and contains three grains labelled in the enlarged inset figure in order to make clear grain 3. The 3D crystal plasticity finite element representation of the oligocrystal with constant grain orientations and geometry through the thickness is also shown in Fig. 10, with the meshing (for the free surface only) given together, in the inset, with that for the ROI. The cyclic R = 0 loading is shown in the figure and is similar to that applied to the single crystals except that no progressively increasing load is applied. A grain map and pole figures for this oligocrystal sample are shown in Fig. 11. The crystal plasticity predicted and SEM observed slip fields developed after ten loading cycles in the ROI are shown in Fig. 12. Slip systems 6 and 9 are active, with system 9 predominating with the highest magnitudes of slip. Slip system 9 is active in both grains 1 and 2 whereas slip system 6 is active in grain 1 alone. The observations of slip activation are in good agreement with crystal plasticity modelling, and Fig. 12 suggests that the grain boundary between grains 1 and 2 has limited effect on constraining slip, while the slip planes activated in the two have differing normal and free-surface manifestation. Region A of
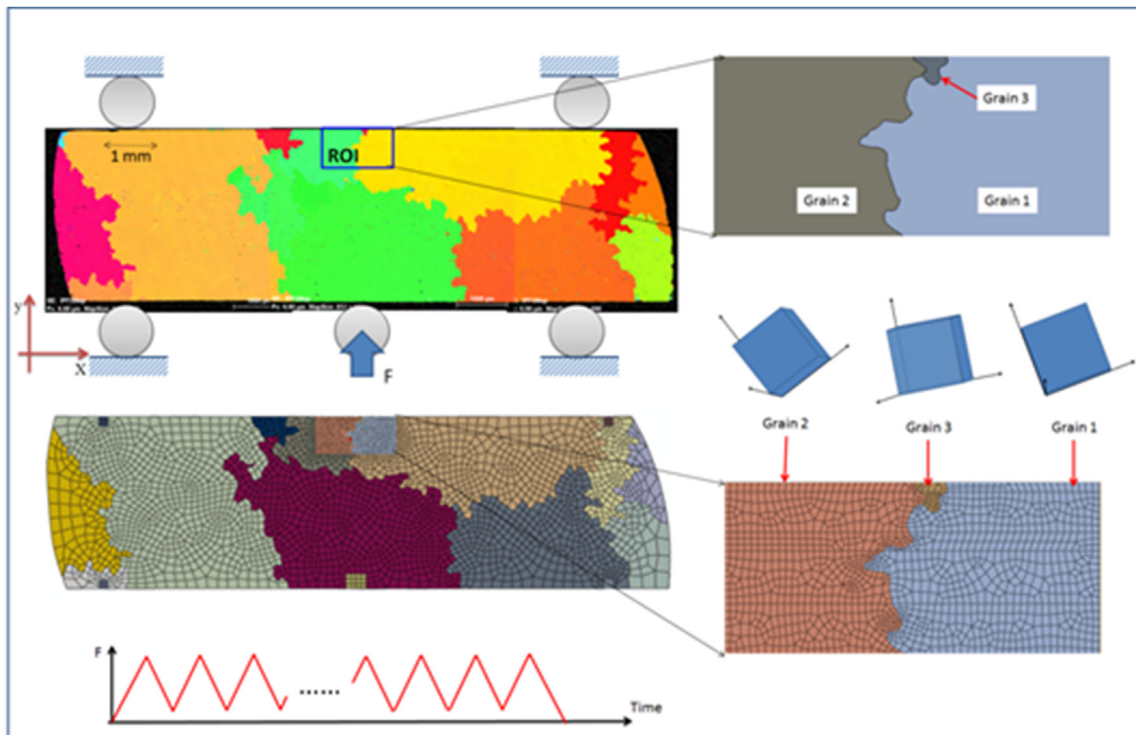
Fig. 10. A large-grained Ni oligocrystal sample 1 with region of interest (ROI) identified and crystallographic orientations of grains 1, 2 and 3 shown, subject to three-point cyclic bend loading shown and the finite element discretization employed for the ROI.

grain 1 identified in the figure is enclosed within parts of grain 2 and might therefore be anticipated to be affected strongly by constraint effects.

However, significant slip (system 6) is observed within Region A in the SEM image, and the crystal model prediction is in good agreement and reflects this. Conversely, grain 3 appears from the SEM image to undergo limited slip which comes from system 9. While the location of grain 3 is within the high bending stress region, the adjacent grains 1 and 2 are better oriented for slip and system 9 is strongly active in both grains, thus accommodating the limited slip in grain 3. The heterogeneity locally with respect to grains 1, 2 and 3 may be seen from further results of the crystal model shown in Fig. 13.

The distribution of effective plastic strain at cycle 20 is given for the ROI together with the distribution of Mises effective stress. The plastic strain distribution reflects the slip contributions and reinforces the localization taking place within grains 1 and 2 which show high strain compared to that in grain 3. The effective stresses carried by the three grains are closer but there is some difference between that in grain 2 and that in grains 1 and 3 indicating that grain 2 is carrying higher in-plane (xy) shear stress (noting that on the free surface shown, $\sigma_{xz} = \sigma_{yz} = 0$). Line graphs of plastic strain and effective stress are also shown in Fig. 13 along the free surface path AA′ at cycles 1, 2 and 20. While not large, there is some local strain accumulation occurring which gives rise to stress redistribution and the cyclically decreasing stresses shown. The marked heterogeneity in strain across grains 1, 2 and 3 is very apparent with a maximum difference of 0.5% between grains 2 and 3.

A second oligocrystal sample also subjected to R = 0 cyclic loading is shown in Fig. 14 together with the corresponding inverse pole figures. This is again a large-grained sample and the ROI lies at the base of the sample, well removed from the contacting loading. The crystal plasticity finite element mesh is shown, together with the locations of points A to G for subsequent analysis. It is noted that a grain boundary lies very close to the location at which the maximum bending stress is anticipated to occur. The crystal model predicted slip and local stress development are first addressed and shown in Fig. 15. Predicted results are shown for cycles 1, 10 and 20 at corresponding (fully loaded) points in each cycle. The heterogeneity of the effective stress within the microstructure is notable, with grain boundaries often showing concentrations. With increasing cycles, the stresses can be seen in the main to show an increasing trend, resulting from the hardening and the progressively increasing strain accumulation due to cycling, which is seen more easily from the accumulated slip fields shown. However, some localized regions show stress relaxation (see later). On the sample free surface where the tensile bending stresses are highest, two grains accommodate most of the plastic strain, but again, significant differences exist across the grain boundary. The left-hand grain shows a quite uniform, high-magnitude strain distribution, whereas that to the right of the near-vertical grain boundary shows very significant localization, with some regions of the same grain showing no slip at all. In fact, the distribution of plastic straining is limited largely in the tensile region to these two grains only. The plastic strain accumulation with cycles is evident and strong and in the left-hand grain, strain accumulation rates of 2.5% over 11 cycles (i.e.
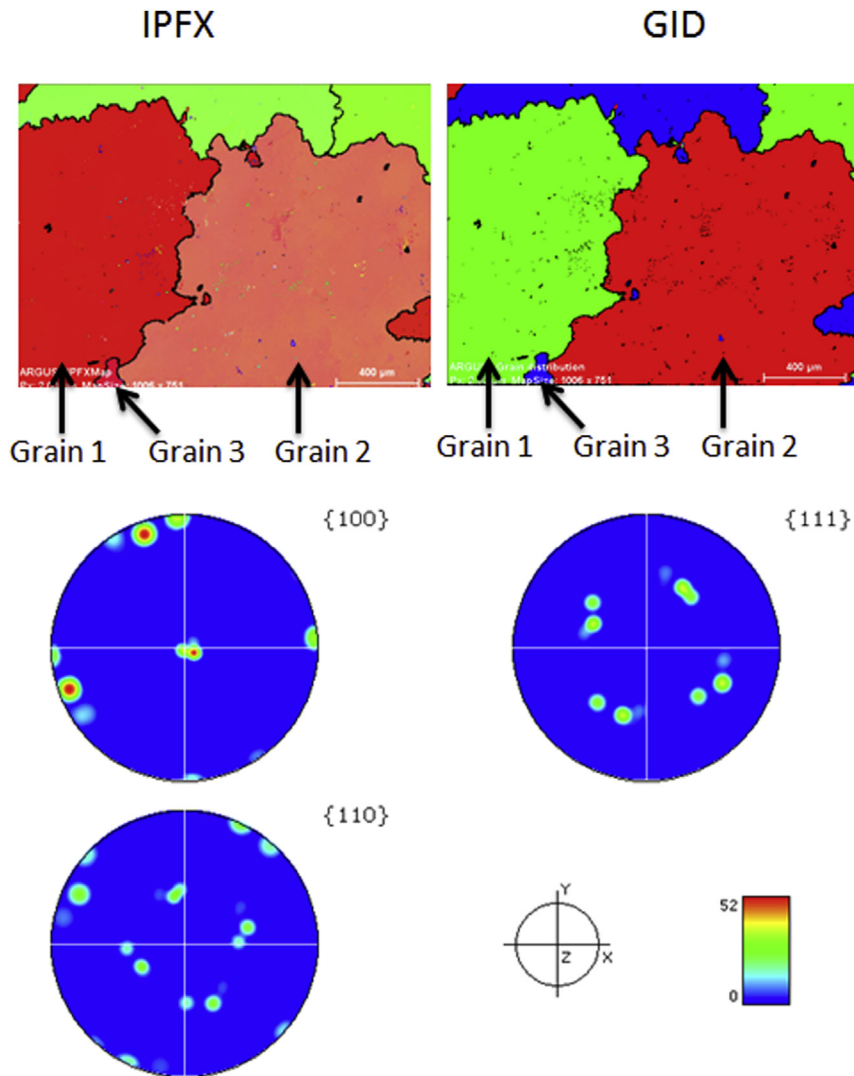
Fig. 11. Grain ID maps and inverse pole figures for the Ni oligocrystal sample 1. Note the beam grain images are inverted with respect to Fig. 10.

0.23%/cycle) are seen. The predicted strain results at cycle 20 are compared directly with DIC-measured strains in the ROI and results are shown in Fig. 16. The DIC measurements have been obtained from the back free surface of the sample, so note that the microstructure image is inverted relative to that shown in Fig. 15. This serves to demonstrate the approximate prismatic nature of the grain structure in this oligocrystal. Reasonably good quantitative agreement is obtained; the strain fields are shown with respect to the same scale bar. The rotations ω_{12}, firstly, reflect that the vertical symmetry anticipated from the continuum macroscale is largely maintained, despite the anisotropy at the grain scale. The DIC measured strains show higher magnitudes of ε_{22} than those predicted. The other strain components show reasonably good qualitative agreement.

A more quantitative comparison is shown in Fig. 17 along the paths indicated within the ROI. With the possible exception of the shear strain along path AA′ (Fig. 17(b)), reasonably good quantitative agreement is seen within the oligocrystal and very wide ranges of strain accumulation are seen. For example, in Fig. 17(a), the bending (ε_{11}) strain along path AA′ is low within the upper grain but up to about 5% in the lower one, demonstrating the very strong heterogeneity and the strong variation from grain to grain successfully captured by the model. The shear strain variations along paths CC′ and DD′ are particularly well represented by the model.

Fig. 18 shows crystal plasticity model results extracted at points A − G on the tensile base of the sample shown in Fig. 14, but firstly, the calculated applied load versus oligocrystal beam mid-displacement is shown in Fig. 18(b) from which macroscale strain accumulation is evident, and that the incremental plastic strain (or displacement) per cycle diminishes and saturates to give a constant small plastic increment per cycle.

The behaviour at the microstructural level is similar but markedly heterogeneous, demonstrated by the plastic strain accumulations at points A to G with time in (b), and the corresponding stress-strain hysteresis loops in (d). Location A shown
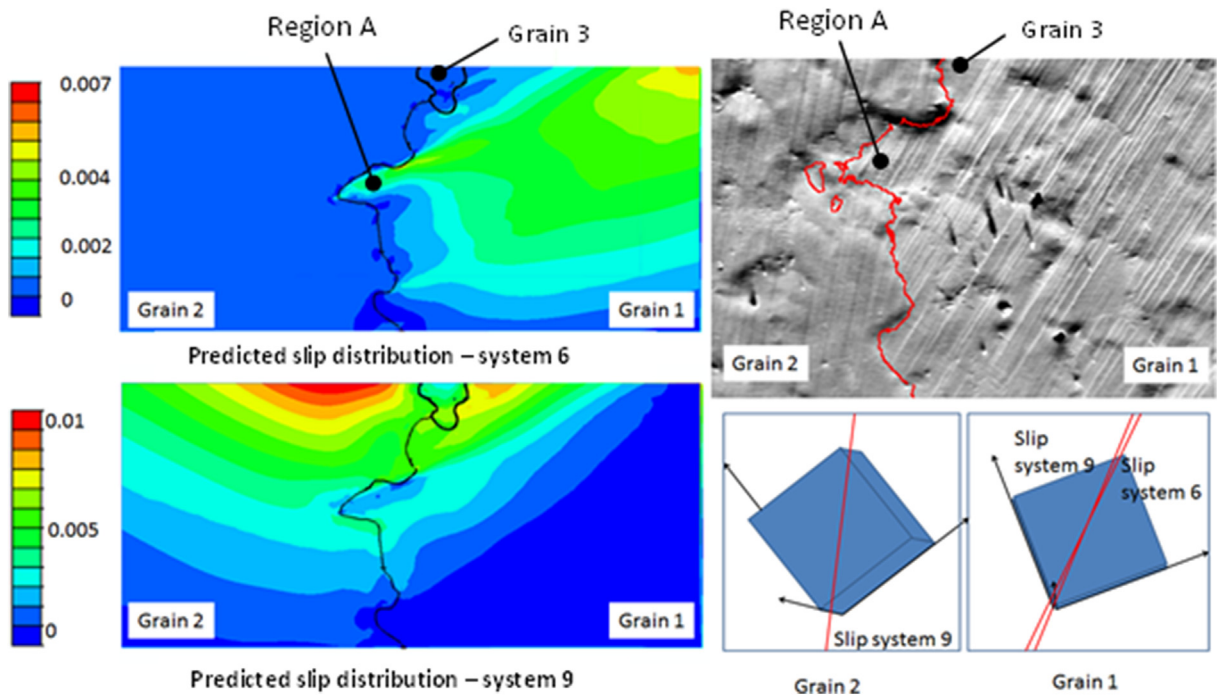
Fig. 12. Comparison of crystal plasticity predicted (top slip system 6, bottom slip system 9) and experimentally observed accumulated slip distributions for the Ni oligocrystal sample 1 in three-point cyclic bend loading.
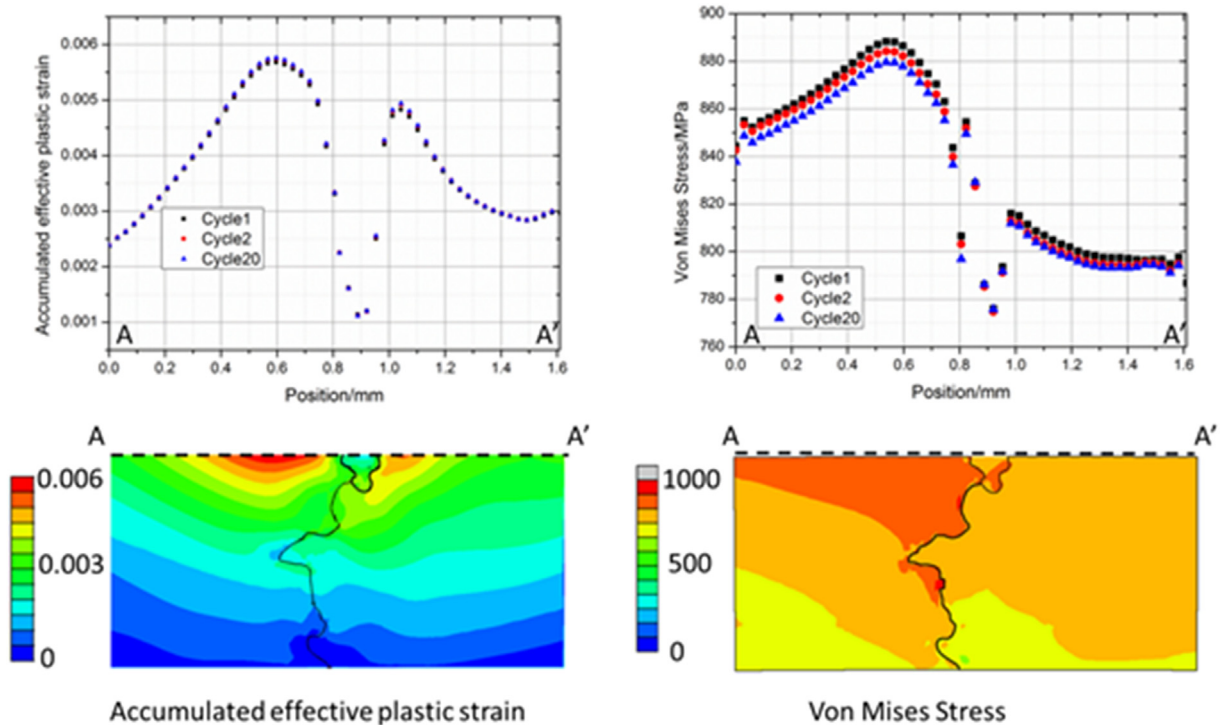

Fig. 13. Crystal plasticity calculated accumulated plastic strain and von Mises stress distributions within the Ni oligocrystal sample 1 ROI demonstrating the effect of the small grain badly orientated for slip.
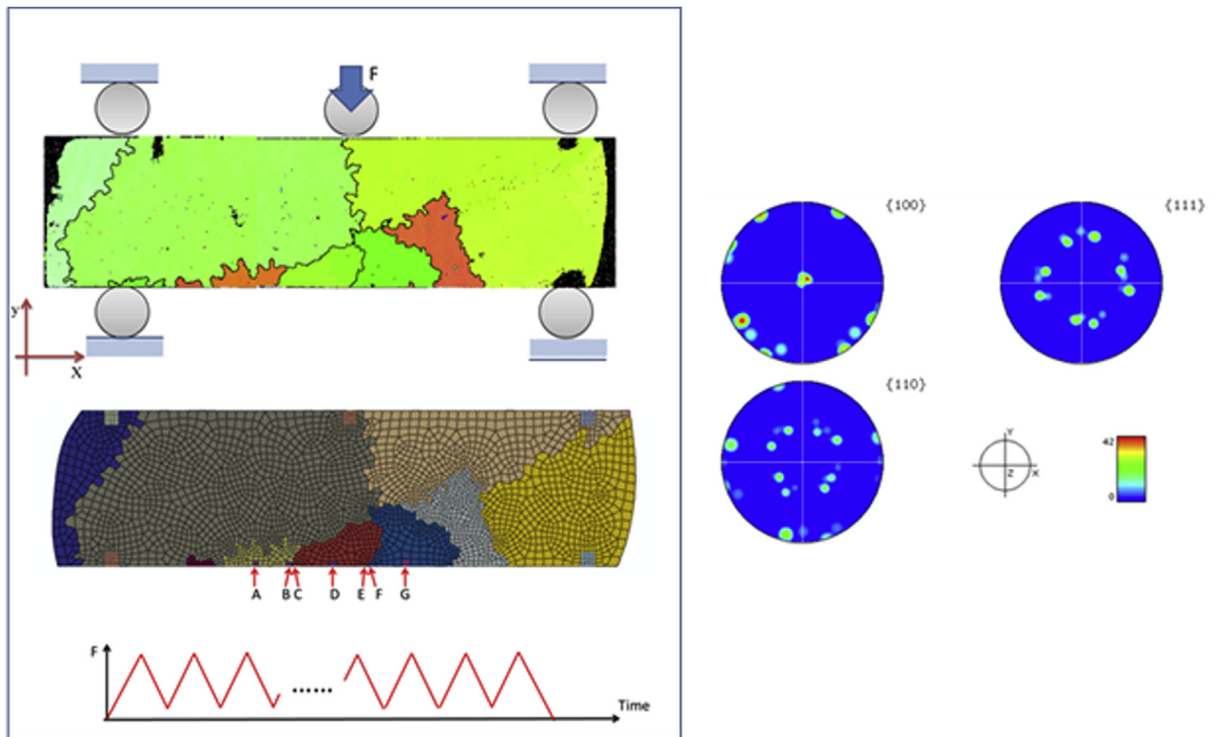
Fig. 14. Large-grained Ni oligocrystal sample 2 (front surface), subject to three-point cyclic bend loading shown and the crystal plasticity finite element discretization employed. Free-surface locations A to G are utilized in subsequent analyses. Insert shows oligocrystal inverse pole figures.
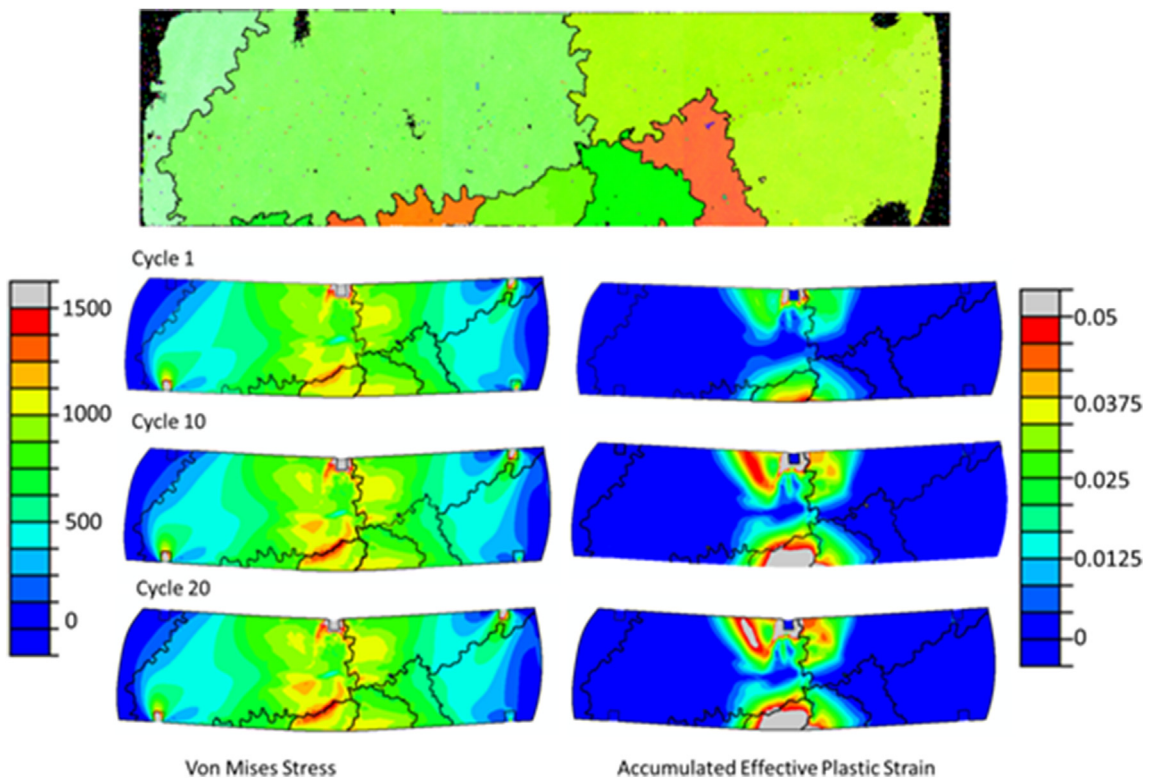

Fig. 15. Crystal plasticity calculated stress (MPa) and accumulated plastic strain in oligocrystal 2 (front surface) after cyclic bend testing at cycles 1, 10 and 20.
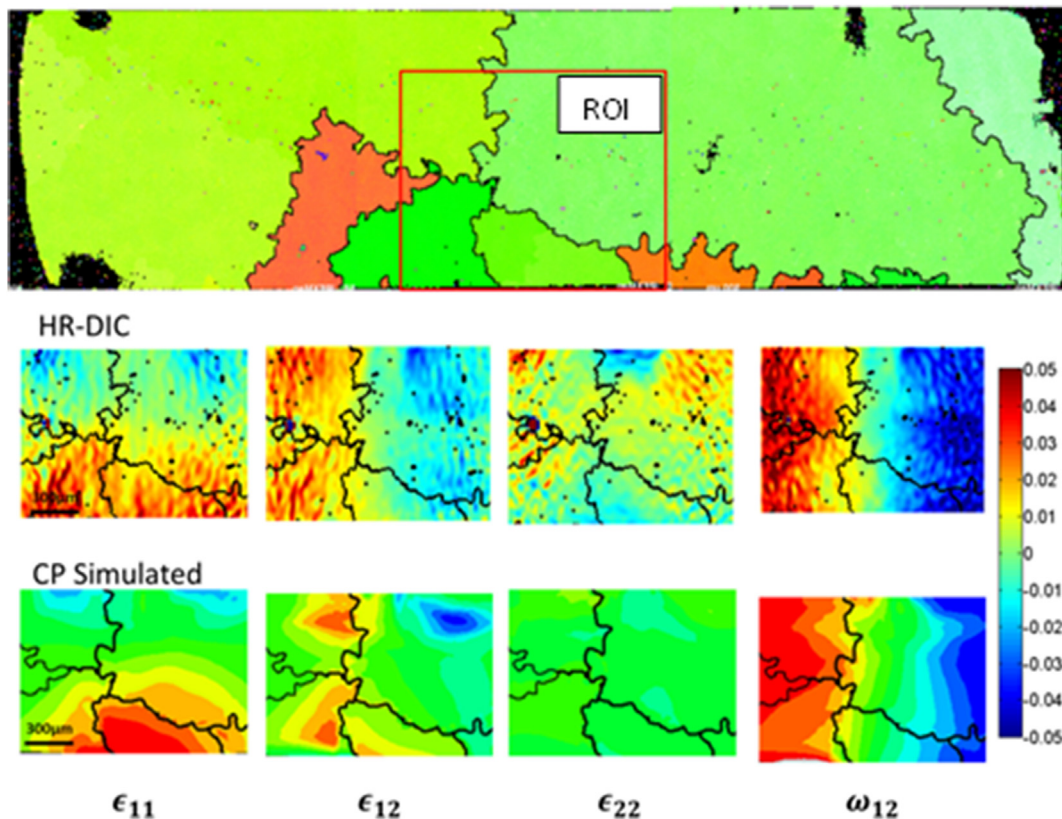
Fig. 16. Direct qualitative comparison of crystal plasticity calculated and DIC-measured strains after cyclic bend testing of Ni oligocrystal 2 (back surface, so note the inversion of microstructure from Fig. 15) for the ROI indicated in the experimental sample (top).

in Fig. 18(a) is at the extreme end of the region within which slip takes place and shows that at this location, slip occurs only in the first cycle and no further plasticity occurs giving elastic shakedown. Locations B and C show very similar strain accumulation and are in close proximity and show plastic shakedown to approximately steady hysteresis response. They are on either side of a grain boundary, thereby each sitting within a different grain, and their respective behaviours are dramatically different. In Fig. 18(d), location B shows the elastic-plastic response in the first cycle is followed by mean stress relaxation such that by the 20th cycle, the stress-strain hysteresis loop is about symmetric about a zero mean stress. For this reason, there is little or no further accumulation of plastic strain. Location C, however, is different in that stress relaxation does not occur and a strong mean stress continues to be maintained giving rise to a continued incremental plastic straining. Locations D, E and F are well-orientated for slip and show similar behaviours. A large accumulation of plastic strain occurs in the first cycle during which some hardening takes place, after which strain accumulation occurs which progressively reduces with cycles until a steady state strain increment appears to be achieved. The range of behaviours observed — including that which occurs in close proximity but either side of a grain boundary — is rather remarkable; the range includes the purely elastic response, elastic shakedown following plasticity through to progressive strain accumulation, all occurring within a few grains.

5. Discussion and conclusions

Slip activation and plastic strain development have been found to be profoundly heterogeneous in CMSX4 single crystals and also in the MAR002 oligocrystals considered. The initiation of slip in the single crystals was found to be highly localized in bands, of about 1—2 μm thickness and 30 μm separation. With increasing loading, the bands thickened to develop a more uniform field of straining which could be captured with crystal plasticity modelling. The plastic strain fields so developed in single crystals subject to cyclic bending are non-symmetric, despite the symmetry of loading, and vary depending on the orientation of the crystal principal axes with respect to the principal loading axes. A consequence is that the localization of slip within a deforming single crystal also depends strongly on orientation. Multiple slip is seen from experimental SEM observations as well as single slip. The activation of slip, be it for a single system or multiple systems concurrently, is captured by crystal plasticity modelling with accurate spatial resolution. Similarly, the nonsymmetric and heterogeneous strain fields developed within single crystals of differing crystallographic orientation, are also captured.
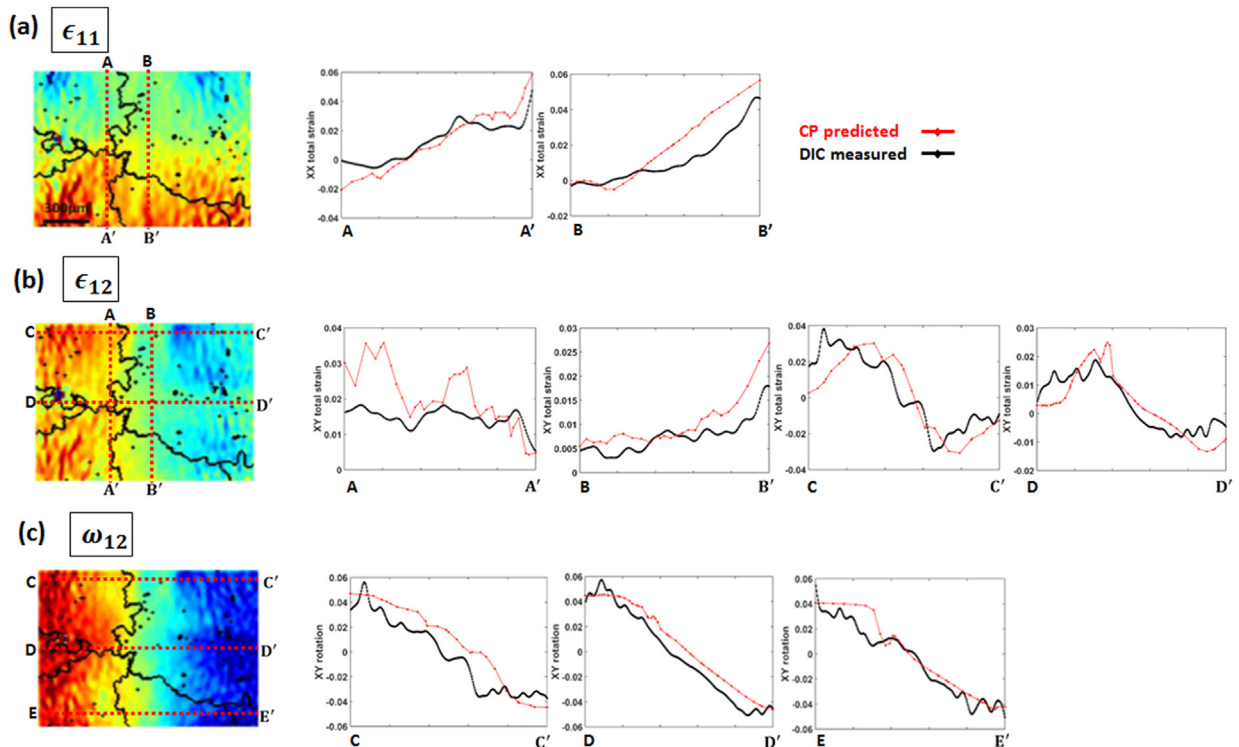
Fig. 17. Quantitative comparison of crystal plasticity calculated (red) and DIC-measured (black) strains and rotations after cyclic bend testing (at cycle 20) of Ni oligocrystal 2 (back surface) for the ROI indicated in the experimental sample. (For interpretation of the references to colour in this figure legend, the reader is referred to the web version of this article.)

The introduction of grain boundaries through consideration of oligocrystal MAR002 provides the opportunity to examine the role played by boundaries in comparison to the single crystal behaviour. Firstly, crystal modelling validated against single crystal behaviour was shown to reproduce the experimentally observed slip activation and the resulting distributions of heterogeneous straining in the oligocrystals. For example, the heterogeneity in slip and strain developed by the presence of a small grain badly orientated for slip but between two grains well-orientated was experimentally observed and replicated well by the model. In another example where grain constraint effects in relation to compatibility of strains were anticipated to be severe, in fact the experimental SEM observations showed limited effect on slip activation and the same behaviour was captured by the model. Within the oligocrystal samples tested, some grains within the high bending stress region developed high and reasonably uniform plastic strains, whereas other grains showed very considerable heterogeneity of slip. In the latter, one zone of the grain developed severely slipped regions whereas other zones did not, argued to result from the constraint imposed by surrounding grains which in this instance were of the appropriate orientation to change the local stress states and hence inhibit slip. This behaviour was also captured by the crystal model.

With reasonable confidence in a microstructure-level predictive capability, it becomes possible to investigate aspects of microstructural behaviour which remain difficult to examine experimentally. The heterogeneity and localization of slip has already been much referenced (Carroll et al., 2013; Miao et al., 2012; Lim et al., 2014; Pinna et al., 2015; Tasan et al., 2014; Weaver et al., 2016), and is likely key to extreme processes such as fatigue crack nucleation. But knowledge of localization, whilst important, is not sufficient. What is also needed is knowledge of microstructure-level local stress, GND and SSD density, together with slip in order to access information such as local stored energy (Jiang et al., 2016a; Wan et al., 2014, 2016) or other fatigue indicator parameters (FIPs). Hence, ideally, full hysteresis loop information over loading cycles is needed at the microstructural hotspots. This is because some locations within the microstructure shakedown elastically, others plastically (i.e. giving steady hysteresis loops) but other locations continue to ratchet, leading to the progressive incremental increase in slip accumulation, hardening through SSD interactions, the establishment of plastic strain gradients and GND structures with the consequence of rising stresses potentially driving nucleation (Zhang et al., 2016; Zhang et al., 2015a; Jiang et al., 2016a). Other locations, however, show mean-stress relaxation and the termination of strain accumulation, thus changing the propensity for defect nucleation. The crystal plasticity model in the present study, verified reasonably well against the single and oligocrystal measured behaviour, shows that the range of complex behaviours just outlined are indeed developed within the oligocrystal microstructures studied, and reinforce the need for appropriate experimental
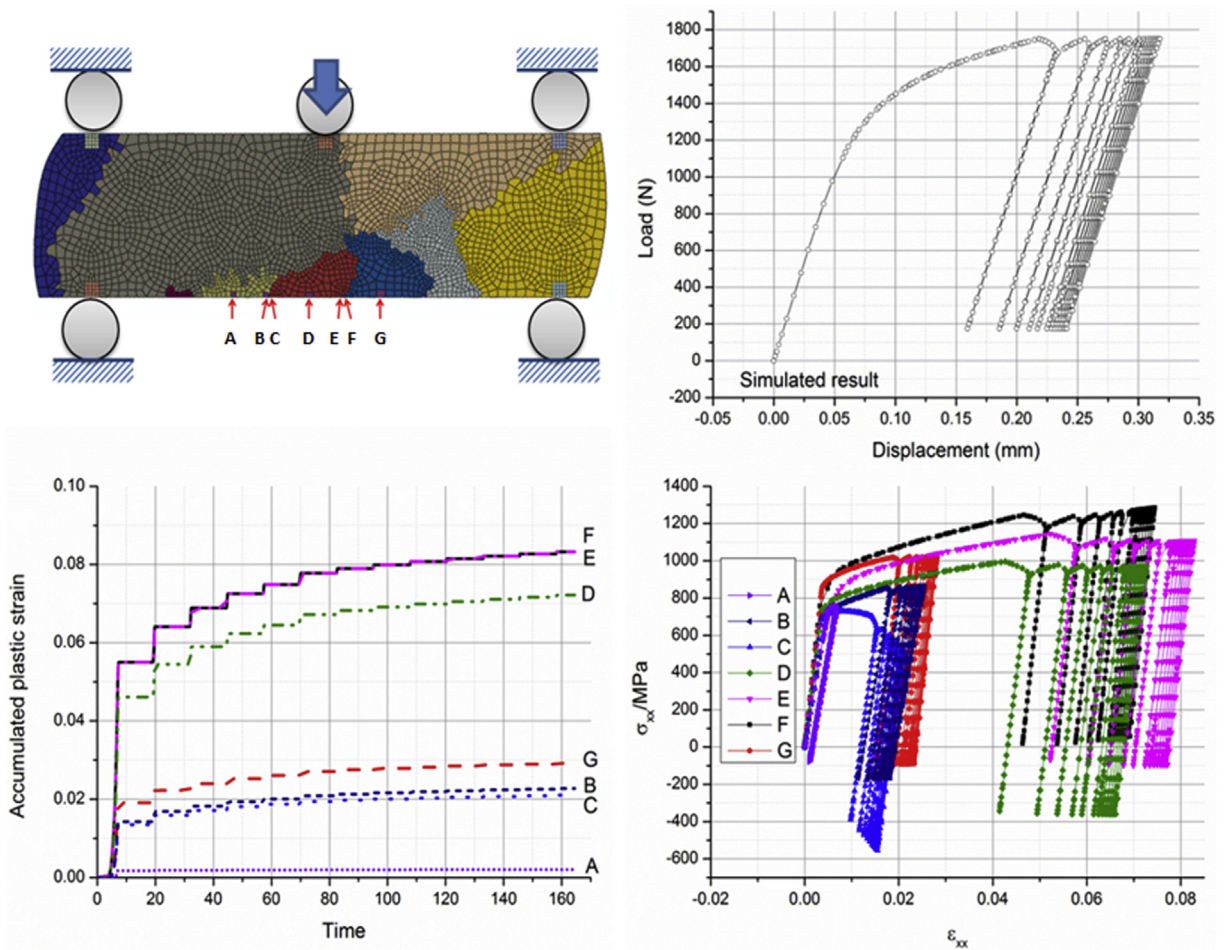
Fig. 18. (a) Oligocrystal sample 2 loading (front surface) with (b) calculated macroscale force versus displacement giving rise to (c) the accumulated plastic strains at the beam free-surface locations shown and (d) the corresponding local stress–strain hysteresis loops obtained at the same locations.

microstructure-level investigations to measure them so that further model validation may be achieved. A good example of why this is potentially important in fatigue has been reported above where two locations either side of a grain boundary show both similar and markedly differing responses. The similarity was that the rate of accumulated plastic strain was about the same at both, but interestingly, at one location, mean-stress relaxation occurred, in effect terminating subsequent plastic strain accumulation, whereas at the other adjacent location, no such relaxation occurred and plastic strain accumulation continued. It is reasonable to argue that the non-slipping grain location acts to inhibit the slip at the adjacent location, generating stress which progressively increases with cycles until such time that it is high enough to generate local void nucleation and a subsequent fatigue crack. Independent work addressing microstructural fatigue hotspots on the basis of a stored energy density (thereby needing knowledge of transient slip, stress and GND/SSD densities) has indicated that grain boundaries are preferential fatigue crack nucleation sites, e.g. over triple junctions. Where other key microstructural features are present (e.g. agglomerates in PM nickel alloys), then these locations are anticipated to drive crack nucleation processes (Zhang et al., 2016; Zhang et al., 2015a; Jiang et al., 2015, 2016a).

The motivation for this paper was based on the establishment of mechanistic understanding towards fatigue crack nucleation (Dunne, 2014; Chan, 2010; Sangid, 2013; Stein et al., 2014) in a simple class of nickel alloys. The study completed has so far addressed slip heterogeneity and localization in both single and oligocrystals over numbers of loading cycles insufficient in order to cause crack nucleation. However, a verified modelling methodology now exists, together with a range of nickel single and oligocrystal samples for which details of the slip activation and localization are now known. These same samples, complemented by others, have been subjected to further cycling in order to nucleate and grow microstructurally sensitive cracks such that crack nucleation locations, cycles to crack nucleation, and crack growth rates are known. The crystal plasticity model presented in this paper, coupled with a stored energy density criterion for fatigue crack nucleation, in conjunction with the results reported in this paper, are now being studied and will be the subject of a subsequent paper.

Acknowledgements

References

Bonacuse, P.J., Kantzos, P., Telesman, J., Gabb, T., Barrie, R., 2002. Modeling ceramic inclusions in powder metallurgy alloys. In: Fatigue 2002: Proceedings of the Eighth International Fatigue Congress, vol. 2, p. 1339e1346.

Carroll, J.D., Abuzaid, W.Z., Lambros, J., Sehitoglu, H., 2013. On the interactions between strain accumulation, microstructure, and fatigue crack behavior. Int. J. Fract. 180, 223–241.

Chan, K.S., 2010. Roles of microstructure in fatigue crack initiation. Int. J. Fatigue 32, 1428–1447.

Denda, T., Bretz, P.L., Tien, J.K., 1992. Inclusion size effect on the fatigue crack propagation mechanism and fracture mechanics of a superalloy. Metall. Trans. A 23, 519e526.

Dunne, F.P.E., 2014. Fatigue crack nucleation: mechanistic modelling across the length scales. Curr. Opin. Solid State Mater. Sci. 18, 170–179.

Dunne, F.P.E., Rugg, D., 2008. On the mechanisms of fatigue facet nucleation in titanium alloys. Fatigue Fract. Eng. Mater. Struct. 31, 949–958.

Dunne, F.P.E., Walker, A., Rugg, D., 2007. A systematic study of hcp crystal orientation and morphology effects in polycrystal deformation and fatigue. Proc. R. Soc. Lond. 463 (2082), 1467–1489.

Dunne, F.P.E., Rugg, D., Walker, A., 2007. Length scale-dependent, elastically anisotropic, physically-based hcp crystal plasticity: application to cold-dwell fatigue in Ti alloys. Int. J. Plast. 23 (6), 1061–1083.

Dunne, F.P.E., Wilkinson, A., Allen, R., 2007. Experimental and computational studies of low cycle fatigue crack nucleation in a polycrystal. Int. J. Plast. 23 (2), 273–295.

Gabb, T., Telesman, J., Kantzos, P., Bonacuse, P., Barrie, R., 2002. Initial Assessment of the Effects of Nonmetallic Inclusions on Fatigue Life of Powder-metallurgy-processed Udimet (TM) 720.

Huron, E.S., Roth, P.G., 1996. The influence of inclusions on low cycle fatigue life in a P/M nickel-base disk superalloy. Superalloys 1996, 359e368.

Huskins, E.L., Cordero, Z.C., Schuh, C.A., Schuster, B.E., 2015. Micropillar compression testing of powders. J. Mater. Sci. 50, 7058–7063.

Hyzak, J., Bernstein, I., 1982. The effect of defects on the fatigue crack initiation process in two P/M superalloys: Part I. Fatigue origins. Metall. Trans. A 13, 33e43.

Jiang, J., Yang, J., Zhang, T., Dunne, F.P.E., Britton, T.B., 2015. On the mechanistic basis of fatigue crack nucleation in Ni superalloy containing inclusions using high resolution electron backscatter diffraction. Acta Mater. 97, 367–379.

Jiang, J., Yang, J., Zhang, T., Zou, J., Wang, Y., Dunne, F., Britton, T., 2016. Microstructurally sensitive crack nucleation around inclusions in powder metallurgy nickel-based superalloys. Acta Mater. 117, 333–344.

Jiang, J., Zhang, T., Dunne, F.P.E., Britton, T.B., 2016. Deformation compatibility in a single crystalline Ni superalloy. Proc. R. Soc. A 472 (2185).

Li, D.F., Barratt, R.A., O'Donoghue, P.E., Hyde, C.J., O'Dowd, N.P., Leen, S.B., 2016. Micromechanical finite element modelling of thermo-mechanical fatigue for P91 steels. Int. J. Fatigue 87, 192–202.

Lim, H., Carroll, J., Battaile, C., Buchheit, T., Boyce, B., Weinberger, C., 2014. Grain-scale experimental validation of crystal plasticity finite element simulations of tantalum oligocrystals. Int. J. Plast. 60, 1–18.

Miao, J., Pollock, T.M., Jones, J.W., 2009. Crystallographic fatigue crack initiation in nickel-based superalloy René 88DT at elevated temperature. Acta Mater. 57, 5964–5974.

Miao, J., Pollock, T.M., Jones, J.W., 2012. Microstructural extremes and the transition from fatigue crack initiation to small crack growth in a polycrystalline nickel-base superalloy. Acta Mater. 60, 2840–2854.

Pham, M.S., Holdsworth, S.R., 2013. Role of microstructural condition on fatigue damage development of AISI 316L at 20 and 300°C. Int. J. Fatigue 51, 36–48.

Pinna, C., Lan, Y., Kiu, M., Efthymiadis, P., Lopez-Pedrosa, M., Farrugia, D., 2015. Assessment of crystal plasticity finite element simulations of the hot deformation of metals from local strain and orientation measurements. Int. J. Plast. 73, 24–38.

Rugg, D., Dixon, M., Dunne, F.P.E., 2007. Effective structural unit size in titanium alloys. J. Strain Anal. 42 (4), 269–279.

Sangid, M.D., 2013. The physics of fatigue crack initiation. Int. J. fatigue 57, 58–72.

Sangid, M.D., Maier, H.J., Sehitoglu, H., 2011. An energy-based microstructure model to account for fatigue scatter in polycrystals. J. Mech. Phys. Solids 59, 595–609.

Sangid, M.D., Maier, H.J., Sehitoglu, H., 2011. The role of grain boundaries on fatigue crack initiation – an energy approach. Int. J. Plast. 27, 801–821.

Shenoy, M., Kumar, R., McDowell, D., 2005. Modeling effects of nonmetallic inclusions on LCF in DS nickel-base superalloys. Int. J. Fatigue 27, 113e127.

Shenoy, M., Kumar, R., McDowell, D., 2005. Modeling effects of nonmetallic inclusions on LCF in DS nickel-base superalloys. Int. J. Fatigue 27, 113–127.

Stein, C.A., Cerrone, A., Ozturk, T., Lee, S., Kenesei, P., Tucker, H., Pokharel, R., Lind, J., Hefferan, C., Suter, R.M., 2014. Fatigue crack initiation, slip localization and twin boundaries in a nickel-based superalloy. Curr. Opin. Solid State Mater. Sci. 18, 244–252.

Stinville, J.C., Vanderesse, N., Bridier, F., 2015. High resolution mapping of strain localization near twin boundaries in a nickel-based superalloy. Acta Mater. 98, 29–42.

Sweeney, C.A., Vorster, W., Leen, S.B., Sakurada, E., Dunne, F.P.E., 2013. The role of elastic anisotropy, length scale and crystallographic slip in fatigue crack nucleation. J. Mech. Phys. Solids 61, 1224–1240.

Tasan, C.C., Hoefnagels, J.P., Diehl, M., Yan, D., Roters, F., Raabe, D., 2014. Strain localization and damage in dual phase steels investigated by coupled in-situ deformation experiments and crystal plasticity simulations. Int. J. Plast. 63, 198–210.

Wan, V.V.C., MacLachlan, D.W., Dunne, F.P.E., 2014. A stored energy criterion for fatigue crack nucleation in polycrystals. Int. J. Fatigue 68, 90–102.

Wan, V.V.C., Jiang, J., MacLachlan, D.W., Dunne, F.P.E., 2016. Microstructure-sensitive fatigue crack nucleation in a polycrystalline Ni superalloy. Int. J. Fatigue 90, 181–190.

Weaver, J.S., Priddy, M.W., McDowell, D.L., Kalidindi, S.R., 2016. On capturing the grain-scale elastic and plastic anisotropy of alpha-Ti with spherical nanoindentation and electron back-scattered diffraction. Acta Mater. 117, 23–34.

Zhang, T., Collins, D.M., Dunne, F.P.E., Shollock, B.A., 2014. Crystal plasticity and HR-EBSD analysis of full-field polycrystal Ni superalloy strains and rotations under thermal loading. Acta Mater. 80, 25–38.

Zhang, T., Jiang, J., Shollock, B.A., Britton, T.B., Dunne, F.P.E., 2015. Slip localization and fatigue crack nucleation near a non-metallic inclusion in polycrystalline nickel-based superalloy. Mat. Sci. Eng. A 641, 328–339.

Zhang, Z., Cuddihy, M., Dunne, F.P.E., 2015. On rate-dependent polycrystal deformation: the temperature sensitivity of cold dwell fatigue. Proc. R. Soc. A 471 (2181).

Zhang, T., Jiang, J., Britton, T.B., Shollock, B.A., Dunne, F.P.E., 2016. Crack nucleation from combined crystal plasticity modelling, HR-DIC and HR-EBSD in superalloy containing non-metallic inclusions under fatigue. Proc. R. Soc. Lond. 472 (2189).